Manuscript Template

1 **Title**

2 ## Alkylperoxy Radicals are Responsible for the Formation of Oxygenated
3 ## Primary Organic Aerosol

4

5 **Authors**

6 Omar El Hajj[1], Samuel W. Hartness[1], Gregory W. Vandergrift[3], Yensil Park[4], Chase K. Glenn[1],
7 Anita Anosike[1], Annabelle R. Webb[2], Nicholas S. Dewey[2], Anna C. Doner[2], Zezhen Cheng[3],
8 Gurneesh S Jatana[4], Melanie Moses-DeBusk[4], Swarup China[3], Brandon Rotavera[1,2]*, Rawad
9 Saleh[1]*

10

11 **Affiliations**

12 [1] School of Environmental, Civil, Agricultural, and Mechanical Engineering, University of Georgia; Athens, GA 30602, USA.

13 [2] Department of Chemistry, University of Georgia; Athens, GA 30602, USA.

14 [3] Pacific Northwest National Laboratory; Richland, WA 99352, USA.

15 [4] Energy and Transportation Science Division, Oak Ridge National Laboratory; Oak Ridge, TN 37831, USA.

16 * Corresponding authors. Email: rawad@uga.edu, rotavera@uga.edu

22

23 **Abstract**

24 **Organic aerosol (OA) is an air pollutant ubiquitous in urban atmospheres. Urban OA is**
25 **usually apportioned into primary OA (POA), mostly emitted by mobile sources, and**
26 **secondary OA (SOA), which forms in the atmosphere due to oxidation of gas-phase**
27 **precursors from anthropogenic and biogenic sources. By performing coordinated**
28 **measurements in the particle phase and the gas phase, we show that alkylperoxy radical**
29 **chemistry that is responsible for low-temperature ignition also leads to the formation of**
30 **oxygenated POA (OxyPOA). OxyPOA is distinct from POA emitted during high-**
31 **temperature ignition and is chemically similar to SOA. We present evidence for the**
32 **prevalence of OxyPOA in emissions of a spark-ignition engine and a next-generation**
33 **advanced compression-ignition engine, highlighting the importance of understanding**
34 **OxyPOA for predicting urban air pollution patterns in current and future atmospheres.**

35 **Teaser**
36 The discovery of an unexpected source of oxygenated organic aerosol is reported.

37

38 **MAIN TEXT**
39 **Introduction**
40 Atmospheric aerosols exhibit profound impacts on air quality and the climate. Commonly referred to as particulate
41 matter (PM) in the public-health community, aerosols are associated with various health effects and inflict the highest
42 social cost among air pollutants (*1, 2*). Unlike greenhouse gases, which perturb the atmospheric radiative balance via
43 a straightforward mechanism (the greenhouse gas effect), aerosols exhibit complex direct and indirect interactions
44 with atmospheric radiation, rendering them the largest contributor to uncertainty in climate calculations (*3*). Organic
45 aerosol (OA) constitutes the majority of submicron aerosol mass in both urban and rural atmospheres (*4*). A large
46 fraction of OA forms via diverse gas-phase chemical reaction pathways that produce molecules with low volatilities,
47 favoring particle formation via condensation. Such reactions occur during combustion (*5*) leading to the formation of
48 primary organic aerosol (POA), as well as in the atmosphere (*6, 7*) leading to the formation of secondary organic
49 aerosol (SOA). Though OA mass concentrations in the atmosphere can be quantified with relatively high confidence,

50 detailed speciation of OA is challenging. In response, atmospheric chemists have devised creative techniques that
51 allow grouping OA into different categories and linking these categories to sources (*4*). The most prevalent
52 categorization framework is based on factor analysis applied to aerosol mass spectrometer (AMS) measurements (*8,*
53 *9*). Under this framework, hydrocarbon-like OA (HOA) represents OA with low oxygen content (O/C < 0.1), while
54 oxygenated OA (OOA) represents OA with high oxygen content (0.25 < O/C < 1). The current consensus is that
55 OOA is predominantly composed of SOA, while urban POA, emitted from the combustion of hydrocarbon fuels (e.g.
56 vehicle emissions), is HOA (*4*). Here we show that hydrocarbon combustion can emit what we refer to as oxygenated
57 POA (OxyPOA), which retains chemical properties similar to those of SOA. We present results from laboratory
58 experiments that link OxyPOA formation to low-temperature combustion chemistry (*10-12*). We also provide
59 evidence of OxyPOA in emissions from spark-ignition and next-generation advanced compression-ignition engines,
60 illustrating the relevance of elucidating OxyPOA formation to understanding OA pollution in current and future
61 urban atmospheres.
62
Results

64   **Difference in POA emitted from first-stage and second-stage ignition**
65 Figure 1 shows results from chemical analysis of POA emitted from the controlled combustion of *n*-pentane and *n*-
66 heptane. We distinguish between 'first-stage POA,' which formed at relatively low temperatures (550 K – 650 K)
67 where reactions of peroxy radicals (RO_2) dominate, and 'second-stage POA,' which formed at relatively high
68 temperatures (> 1000 K) (see fig. S1 in the supplementary materials). Traditionally, only second-stage POA has been
69 thought to constitute POA emissions from the combustion of hydrocarbon fuels, whereas first-stage POA was only
70 recently discovered (*13*). Therefore, it is imperative to set the appropriate context for the results. Second-stage POA
71 forms at relatively high temperatures (> 1000 K) and is equivalent to 'incipient soot' in combustion science
72 terminology (*14*). It is comprised of polycyclic aromatic hydrocarbons (PAHs) and aliphatic species (*5*) and therefore
73 falls strictly under HOA (*4*). With further increase in temperature, the organic molecules that comprise second-stage
74 POA transform into mature soot (*14*), which is largely equivalent to black carbon (BC) in atmospheric science
75 terminology (*15*). BC is a strong light-absorber and a leading contributor to global warming (*15*). Second-stage POA
76 can also be light-absorbing and is categorized as brown carbon (BrC) (*16*). For these reasons, the formation and
77 physicochemical properties of second-stage POA have been extensively studied by both combustion scientists and
78 atmospheric scientists (*5, 13, 16, 17*).
79 Some hydrocarbon fuels, including *n*-pentane and *n*-heptane, exhibit two-stage ignition behavior (*18, 19*), with first-
80 stage ignition occurring at relatively low temperatures (550 K – 750 K). Discovery of first-stage ignition in the mid-
81 twentieth century was motivated by efforts to understand the cause of engine knock in spark-ignition engines (*20,*
82 *21*). Furthermore, the importance of first-stage ignition in advanced compression-ignition (ACI) engines that rely on
83 low-temperature combustion (LTC) remains an impetus for unveiling chemical kinetics of RO_2. As part of a complex
84 degenerate chain-branching mechanism, RO_2 isomerization to (carbon-centered) QOOH radicals and subsequent
85 reactions are the focal points for understanding chain-branching reactions in combustion (*12, 22*). However, while the
86 dynamics of two-stage ignition chemistry is known to rely on QOOH-mediated reactions below 1000 K, the
87 concomitant production of organic molecules with volatilities low enough to condense and form OA (i.e. first-stage
88 POA) has only recently been reported (*13*).
89 The second-stage POA generated in our experiments was detected by laser desorption ionization mass spectrometry
90 (LDI-MS) and exhibited clusters of peaks separated by 12 u (fig. S2 in the supplementary materials), which are
91 characteristic signatures of PAHs. Similar spectra have been reported for POA extracted from flames (*23, 24*) and
92 pyrolysis of hydrocarbons (*25, 26*). The clusters of peaks with 12 u separation have been shown to correspond to two
93 series associated with even carbon numbers (usually major peaks) and odd carbon numbers (usually minor peaks),
94 each separated by 24 u, with 12 u offset between them. At large molecular sizes, the minor peaks become less
95 prominent and can disappear from the spectra (*16, 24, 27*), leaving the major peaks with 24 u separation (Fig. 1).
96 Being non-polar, the second-stage POA molecules were not efficiently ionized by electrospray ionization (ESI) and
97 were thus not detected by ultra-high resolution ESI mass spectrometry (ESI-MS). Conversely, the first-stage POA
98 was transparent to LDI-MS but was detected by ESI-MS, indicating that the first-stage POA did not include PAHs
99 and was comprised of polar compounds that were efficiently ionized by ESI. The first-stage POA had an average O/C
100 of 0.65 and 0.56 for *n*-pentane and *n*-heptane, respectively, and thus falls under OOA, a category previously reserved
101 for SOA (*4, 28, 29*). Furthermore, ESI-MS spectra show repetitive clusters of peaks separated by 14 u, which is
102 indicative of oligomer formation (*30*), another feature usually associated with SOA (*31-33*) and is further explored in
103 the subsequent section. It is possible that the first-stage POA included some reduced species that were not detected by
104 ESI-MS, but the fact that it was completely transparent to LDI-MS indicates that reduced species, if any, did not
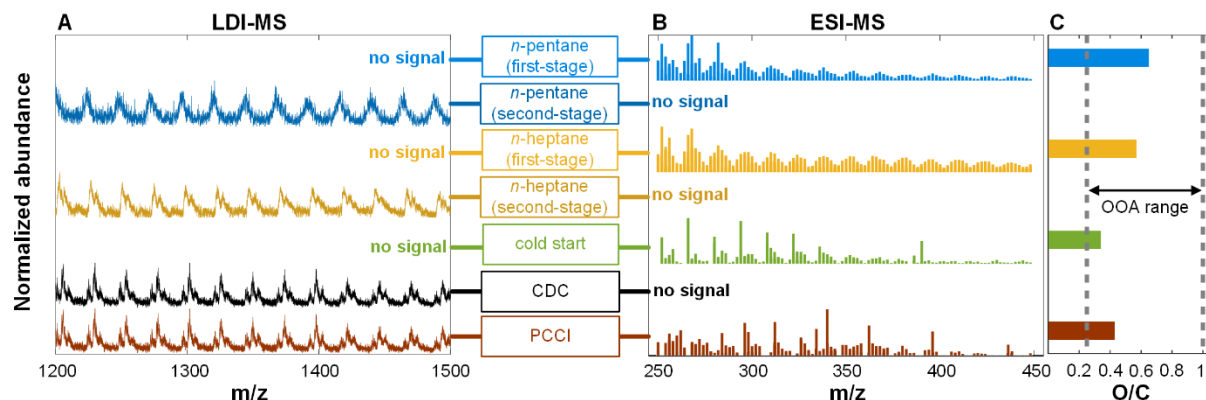105 constitute a substantial fraction.

Fig. 1. Mass spectrometry analysis of POA emissions from controlled combustion of *n*-pentane and *n*-heptane, a spark-ignition engine operated at simulated cold-start conditions, and a compression-ignition engine operated at steady-state conditions using either conventional diesel combustion (CDC) strategy or an advanced compression-ignition (ACI) strategy (premixed charge compression ignition – PCCI). The temperature of the *n*-pentane and *n*-heptane combustion was controlled to emit either first-stage POA (550 K – 650 K) or second-stage POA (1100 K – 1300 K) (see supplementary materials). **(A)** Mass spectra obtained using LDI-MS. **(B)** Mass spectra obtained using ESI-MS. **(C)** Average O/C of the molecules detected by ESI-MS. The *n*-heptane first-stage POA was also analyzed using high resolution nanospray desorption electrospray ionization (nano-DESI) mass spectrometry, which yielded mass spectra and average O/C (0.57) consistent with ESI-MS (fig. S3).

These results demonstrate a marked difference in chemical characteristics between first-stage POA and traditional hydrocarbon-combustion POA (i.e., second-stage POA), which necessitates distinction between the two. To facilitate use within the context of atmospheric chemistry, we introduce the term 'oxygenated POA' (OxyPOA) to refer to first-stage POA. OxyPOA communicates the most distinct aspect of first-stage POA, namely high O/C, and maintains the same general terminological character used to describe organic aerosol in atmospheric chemistry literature (POA, SOA, HOA, OOA, etc.). We note that OxyPOA is different from oxidized POA (OPOA), a term used to refer to aged POA that has undergone heterogeneous oxidation in the atmosphere (*34, 35*). We also note that even though first-stage POA, or OxyPOA, is essentially organic particulate combustion emissions, it does not form through the high-temperature soot-formation route (*36*) and therefore should not be subsumed under the term 'incipient soot' (*14*). The formation pathways of OxyPOA, described in the subsequent section, differ from those of furans, which involve incorporation of oxygen into PAH structures in the high-temperature region of hydrocarbon flames (*37*). Furthermore, furans and other oxygenated species that form at high temperatures in flames usually have relatively small O/C (*37*), consistent with HOA (traditional hydrocarbon-combustion POA).

Formation pathways of OxyPOA

Collisionally stabilized alkylperoxy radicals (RO_2) traverse unimolecular reactions on potential energy surfaces that include isomerization to carbon-centered QOOH radicals and concerted elimination of HO_2. The former type of reaction is central to chain-branching and can also produce cyclic ether species, as in Fig. 2, in which 2-pentyl undergoes reaction with O_2 to ultimately form 2-methyltetrahydrofuran, which is one of several isomers formed during *n*-pentane oxidation (*38*). Similar to alkyl radicals, cyclic ethers also undergo complex reactions with O_2 (*39-41*). In addition to unimolecular reactions, however, RO_2 radicals can undergo bimolecular reactions including with other RO_2 radicals (*42*). Figure 2 depicts, as an example, a set of reactions of 2-methyltetrahydrofuran that produce highly oxidized, multi-functional intermediates in sequential steps mediated by organic hydroperoxides (ROOH), which result in species of decreased volatility that can partition to the particle phase and contribute to OxyPOA formation.

2-Methyltetrahydrofuran ($C_5H_{10}O$) and 2-methyltetrahydrofuran-3-one ($C_5H_8O_2$) were detected in the gas phase emissions of first-stage *n*-pentane combustion. Both species had temperature-dependent concentration profiles that exhibited similar trends to that of OxyPOA (fig. S4), signifying their role as OxyPOA precursors. As illustrated in Fig. 2, 2-methyltetrahydrofuran-3-one can undergo two additional oxygen-addition steps leading to the formation of $C_5H_6O_3$ molecules (2-methylfuran-3,4(2*H*,5*H*)-dione and 3-oxotetrahydrofuran-2-carbaldehyde), and ultimately $C_5H_4O_4$ molecules (5-methylfuran-2,3,4(5*H*)-trione and 3,4-dioxotetrahydrofuran-2-carbaldehyde). The intermediate $C_5H_6O_3$ molecules were not detected in the gas phase, which is ascribed to their existence at concentrations below the detection limit of our gas-phase instruments. Furthermore, their volatility is appreciably high such that partitioning to the particle phase is precluded (fig. S5). The $C_5H_4O_4$ molecules, however, have volatilities low enough to partition to the particle phase. The *n*-pentane OxyPOA species detected by ESI-MS included a peak at m/z 128.011 that reflects a molecular formula $C_5H_4O_4$, which coincides with 5-methylfuran-2,3,4(5*H*)-trione and 3,4-dioxotetrahydrofuran-2-carbaldehyde in Fig. 2.

153   Other pathways to multi-functional species include the formation of dicarbonyls via oxidation of the tertiary radical
154   of *syn*-2,4-dimethyloxetane, another cyclic ether derived from *n*-pentane (*41*). Fig. S7 illustrates the formation of 2,4-
155   pentanedione ($C_5H_8O_2$) (detected in the gas phase of first-stage *n*-pentane combustion), which undergoes further
156   oxidation to form 2,3,4-trioxopentanal and 2,4-dioxopentanedial. Both species have molecular formula $C_5H_4O_4$,
157   which coincides with the m/z 128.011 peak detected in the particle phase.
158   It is worth noting that the chemical composition of OxyPOA shares some similarity with highly oxygenated organic
159   molecules (HOMs) (*43*) by containing multiple oxygen atoms in a hydrocarbon structure. However, the two are
160   differentiated by the formation mechanisms: OxyPOA arises from QOOH-mediated, cyclic-ether derived reaction
161   pathways during low-temperature combustion, whereas HOMs form via autoxidation involving RO_2 radicals in the
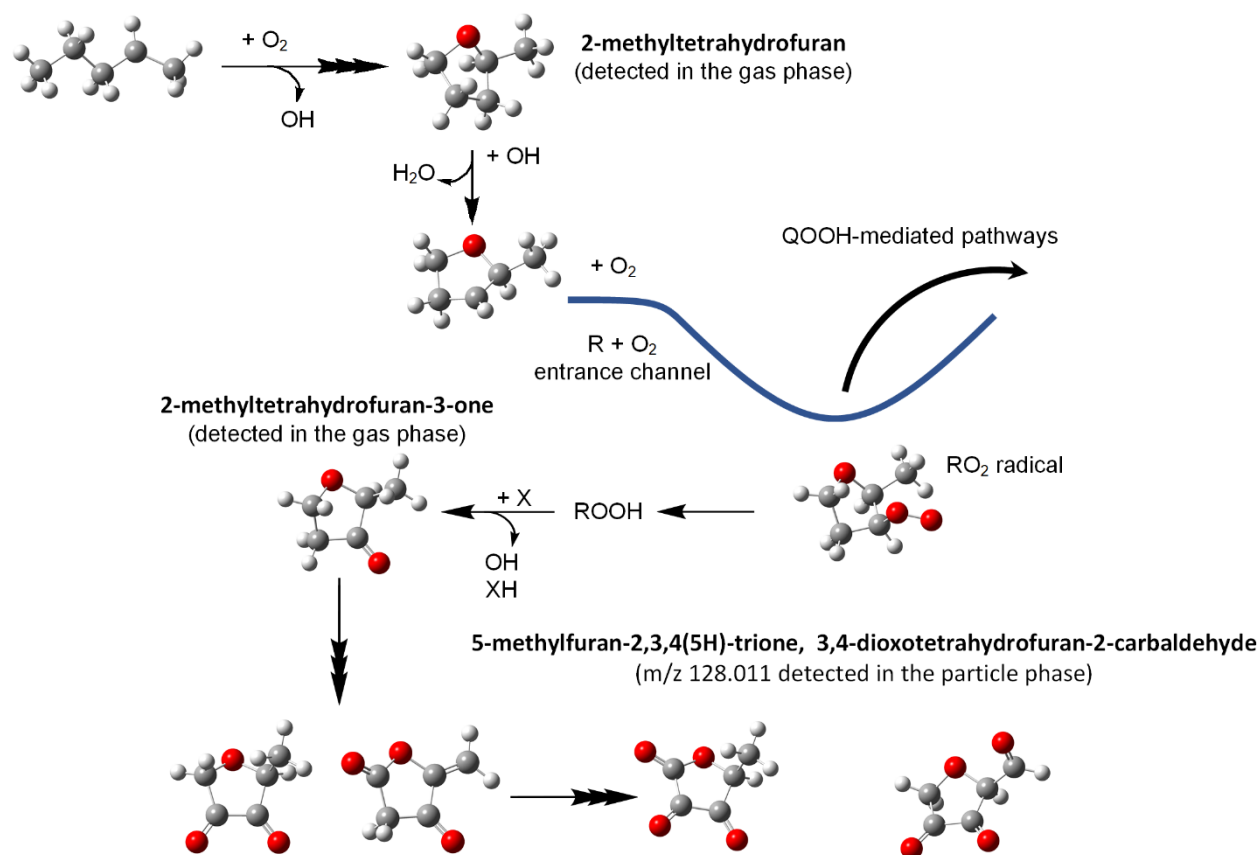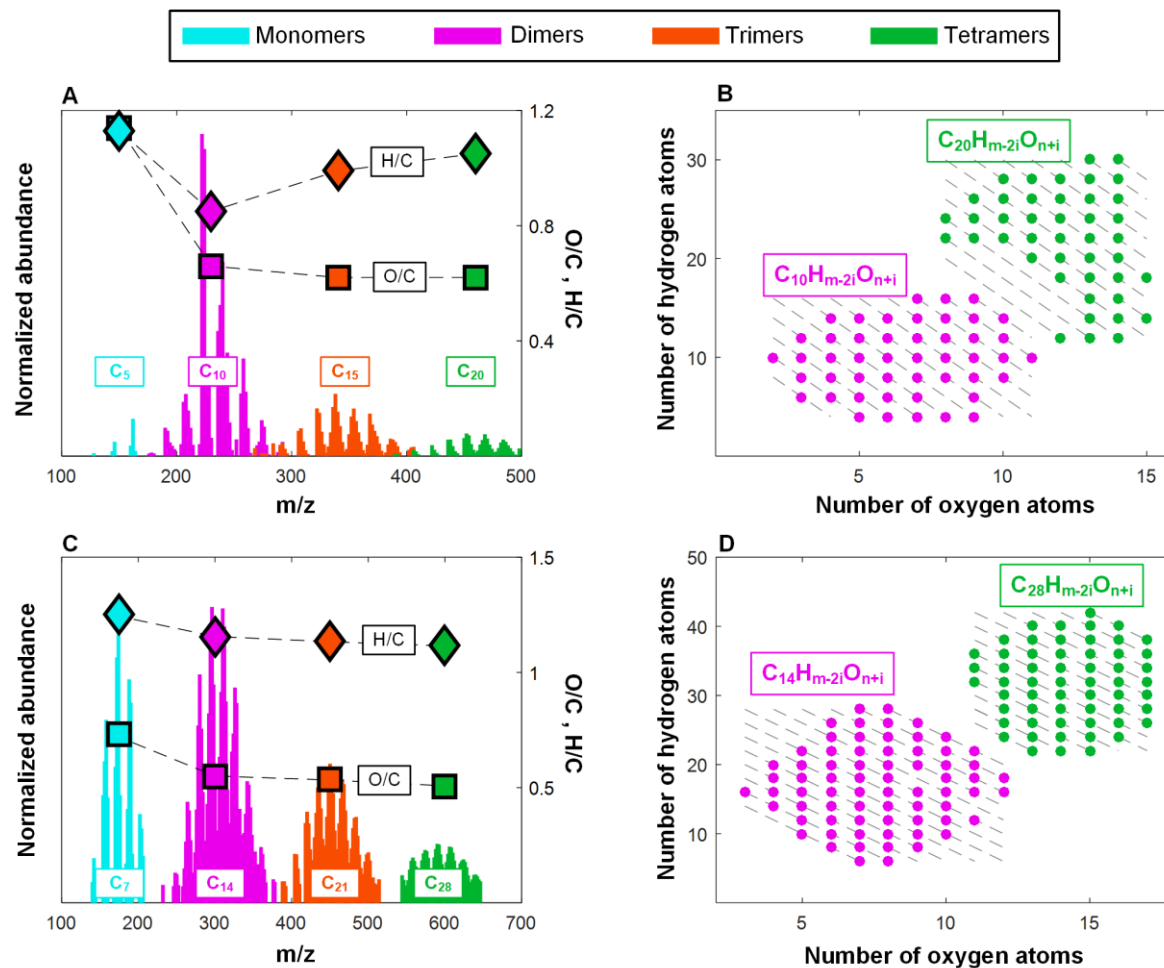162   atmosphere and are contributors to SOA (*43*).
163

164
165   **Fig. 2.** Pathway for OxyPOA formation from gas-phase precursors produced during first-stage combustion of *n*-
166   pentane. Oxidation of 2-pentyl produces 2-methyltetrahydrofuran, a cyclic ether, via a QOOH-mediated reaction.
167   Subsequent H-abstraction and O_2-addition produces cyclic ether peroxy radicals (RO_2), such as 2-methyl-
168   tetrahydrofuranyl-3-peroxy, which can undergo additional QOOH-mediated reactions or act as a hydrogen abstractor
169   to produce ROOH. Abstraction of tertiary hydrogen from ROOH and barrierless O–O scission of the resultant
170   carbon-centered radical, carbonyl-substituted species are produced coincident with OH in a chain-propagating step
171   (*42*). Subsequent oxidation of species such as 2-methyl-tetrahydrofuran-3-one yields condensable species that form
172   OxyPOA. The RO_2 well-depth, shown arbitrarily submerged, is typically 35 kcal/mol exothermic relative to the R +
173   O_2 entrance channel. X denotes a generic radical and XH denotes a closed-shell hydrogen donor. Fig. S6 in the
174   supplementary materials provides a detailed reaction scheme for other pathways involving RO_2 radicals that occur
175   during low-temperature combustion.
176
177   Supported by species detected in the gas phase and particle phase of the *n*-pentane first-stage combustion emissions,
178   the schemes in Fig. 2 and fig. S7 provide viable pathways for OxyPOA formation from gas-phase precursors.
179   However, this alone cannot explain the large molecular sizes observed in the mass spectra of OxyPOA species (Fig. 1
180   and fig. S3). Limited by the scarcity of small hydrocarbon radicals at LTC conditions, such as vinyl and propargyl, it
181   is unlikely for gas-phase reactions to produce species with carbon numbers larger than that of the parent hydrocarbon.
182   We hypothesize that the critical final step in OxyPOA formation is molecular growth by oligomerization. Formation
183   of oligomers not only renders the molecules in the particle phase less volatile, but also provides a condensation sink
184   for more monomers to condense and oligomerize, thus creating a feedback mechanism that promotes condensational
185   particle growth. We provide two levels of evidence for the prevalence of oligomers in OxyPOA: (i) patterns in the
186   ESI-MS spectra, and (ii) response to perturbation in gas-particle equilibrium partitioning.

Fig. 3. Evidence for oligomer formation from ESI-MS analysis. (**A** and **C**) ESI-MS spectra of OxyPOA in *n*-pentane and *n*-heptane combustion that isolate C_5 monomers (*n*-pentane, **A**) and C_7 monomers (*n*-heptane, **C**) and oligomers with carbon numbers that are multiples of 5 and 7, respectively. Also shown are the average H/C and O/C of the monomers and the oligomers. (**B** and **D**) Number of hydrogen atoms versus number of oxygen atoms of the dimers and tetramers. (**B**) All the dimers and tetramers in the *n*-pentane OxyPOA belong to families with the general formula $C_{10}H_{m-2i}O_{n+i}$ and $C_{20}H_{m-2i}O_{n+i}$ (dashed gray lines), respectively. (**D**) All the dimers and tetramers in the *n*-heptane OxyPOA belong to families with the general formula $C_{14}H_{m-2i}O_{n+i}$ and $C_{28}H_{m-2i}O_{n+i}$ (dashed gray lines), respectively. Results consistent with those in panels **C** and **D** for *n*-heptane were obtained using nano-DESI mass spectrometry (fig. S3).

Mass spectra of oligomers previously observed in SOA are characterized by broad groupings, with each grouping comprised of clusters of equidistant peaks (*32*). Due to the high diversity of monomer combinations, the broad groupings are not apparent in the OxyPOA ESI-MS spectra (Fig. 1) but can be observed by isolating monomers with a certain carbon number. Representative results are shown in Fig. 3 for C_5 (*n*-pentane) and C_7 (*n*-heptane) monomers and oligomers with carbon numbers that are multiples of 5 and 7, respectively. These monomers form via first-stage functionalization pathways over which the hydrocarbon backbone remains intact during oxidation, resulting in C_5 (for *n*-pentane combustion) and C_7 (for *n*-heptane combustion) molecules with diverse functionality, including carbonyls and cyclic ethers, which are common products of alkane oxidation (*44, 45*). Isolating molecules with carbon numbers C_{5c} and C_{7c} (c = 1, 2, 3, 4) in the ESI-MS spectra of the *n*-pentane OxyPOA (Fig. 3A) and *n*-heptane OxyPOA (Fig. 3C) reveals oligomer signatures similar to those previously reported for SOA (*32*). Oligomer formation is further evidenced by the relatively small change in H/C and O/C with increasing carbon number, which is consistent with growth by monomer association. One exception is noted for the O/C of the C_5 monomers in *n*-pentane OxyPOA being substantially larger than the oligomers. This can be explained as follows: because of the small carbon number, only the highly functionalized C_5 monomers with high O/C have volatilities low enough (*46*) to partition to the particle phase, resulting in the O/C of the C_5 monomers in the OxyPOA sample being skewed high.

216 The broad groupings of C_{5c} and C_{7c} oligomers exhibit sequences of smaller clusters separated by 14 u. This suggests
217 dominant formation pathways of monomers that include sequential steps with the net result of abstracting two
218 hydrogen atoms and adding one oxygen atom (Fig. 2). Various combinations of these C_5 and C_7 monomers lead to the
219 formation of oligomers with general formulae $C_{5c}H_{m-2i}O_{n+i}$ and $C_{7c}H_{m-2i}O_{n+i}$ (i = 1, 2, 3,…). This is illustrated in Fig.
220 3B and Fig. 3D, which show that all the dimers and tetramers belong to, respectively, $C_{5c}H_{m-2i}O_{n+i}$ and $C_{7c}H_{m-2i}O_{n+i}$
221 families (c = 2,4). The various combinations of monomers (with varying carbon numbers) that form through similar
222 hydrogen-abstraction and oxygen-addition pathways manifest as tightly packed oligomer structures separated by 14 u
223 (Fig. 1).
224 To further confirm the role of oligomerization in OxyPOA formation, we examined the response of *n*-pentane
225 OxyPOA to either dilution with clean air or heating in a thermodenuder. In the absence of oligomers, the extent of
226 evaporation in response to both perturbations would be dictated by internally consistent thermodynamic properties
227 (volatility distribution) of the aerosol components. The presence of oligomers, however, leads to an evaporation
228 response that is limited by the rate of oligomer dissociation, which increases substantially with increasing
229 temperature (*47*). This would manifest as an apparent thermodynamic inconsistency in the aerosol response to the
230 two perturbations: the aerosol would appear more volatile in the thermodenuder perturbation compared to dilution.
231 The dilution perturbation led to minimal evaporation (Fig. 4C), in agreement with equilibrium partitioning
232 calculations using volatility distribution estimated from ESI-MS molecular assignments. This indicates that the
233 estimated volatility distribution, while not meant to be exact, predicted reasonably well the fraction of species that
234 measurably partitioned to the gas phase in response to dilution (intermediate-volatility and semi-volatile compounds).
235 However, equilibrium partitioning calculations using the same volatility distribution severely underestimated the
236 extent of evaporation in the thermodenuder (Fig. 4A). Reproducing the OxyPOA response to the thermodenuder
237 perturbation required substantially shifting the volatility distribution toward higher-volatility components, which
238 would overestimate the extent of evaporation in response to dilution. As we argue above, this seeming
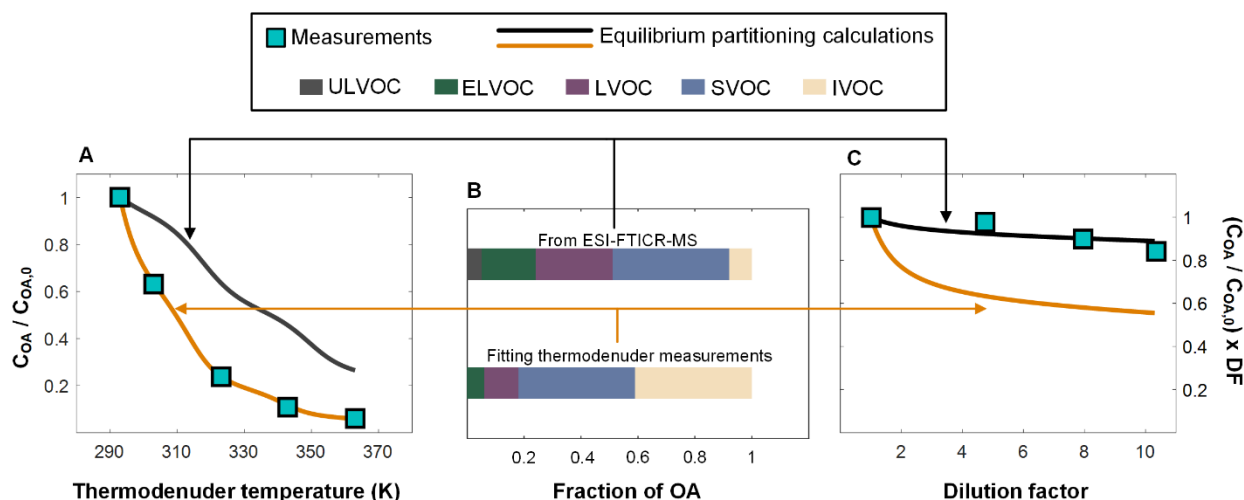239 thermodynamic inconsistency signifies a prominent role of oligomer dissociation (*47*).
240

241
242 **Fig. 4.** Evidence for presence of oligomers in OxyPOA from comparing evaporation measurements of *n*-pentane
243 OxyPOA to equilibrium partitioning calculations. (**A**) Thermodenuder measurements showing the aerosol mass
244 concentration at each temperature (C_{OA}) relative to the aerosol mass concentration at the reference temperature
245 ($C_{OA,0}$). Also shown are equilibrium partitioning calculations using volatility distribution obtained from ESI-MS
246 molecular assignments (black line). The brown line corresponds to equilibrium partitioning calculations using a
247 volatility distribution adjusted to reproduce the measurements. (**B**) Volatility distributions obtained from ESI-MS
248 molecular assignments (top bar) and adjusted to reproduce the thermodenuder measurements (bottom bar). The
249 aerosol components are apportioned into intermediate-volatility (IVOC), semi-volatile (SVOC), low-volatility
250 (LVOC), extremely low-volatility (ELVOC), and ultra-low-volatility (ULVOC) organic compounds. (**C**) Dilution
251 measurements showing C_{OA} at a certain dilution factor (DF) relative to no dilution ($C_{OA,0}$). Dilution leads to a
252 decrease in C_{OA} because of dilution itself as well as evaporation. To isolate the effect of evaporation, the y-axis is
253 scaled by DF, such that the case of no evaporation would show as a horizontal line with a value of 1. Also shown are
254 equilibrium partitioning calculations using volatility distribution obtained from ESI-MS molecular assignments
255 (black line) and volatility distribution adjusted to reproduce the thermodenuder measurements (brown line).

256 **Prevalence of OxyPOA in engine emissions**
257 We performed LDI-MS and ESI-MS analysis on POA samples collected from the emissions of a spark-ignition
258 (gasoline) engine operated at a simulated cold-start condition and a compression-ignition (diesel) engine operated at
259 steady state conditions using either conventional diesel combustion (CDC) strategy or an ACI strategy (premixed

260 charge compression ignition – PCCI). As shown in Fig. 1, the cold-start POA was transparent to LDI-MS but was
261 detected by ESI-MS and exhibited repetitive peaks separated by 14 u with an average O/C within the OOA range.
262 These results indicate that the POA from the simulated cold-start emissions was dominated by OxyPOA. The
263 majority of POA emissions from on-road gasoline vehicles occur during cold-start conditions (48), which are
264 especially important in urban settings where a large share of driving consists of short trips at cold engine conditions
265 (49). Therefore, we expect OxyPOA to be ubiquitous in urban atmospheres.
266 Both CDC and PCCI emitted POA with typical soot-formation signatures identified by LDI-MS, signifying the
267 presence of second-stage POA (Fig. 1). ESI-MS detected species in the PCCI POA but not the CDC POA. Similar to
268 the cold-start POA, the PCCI POA species measured by ESI-MS had O/C within the OOA range and the spectra
269 exhibited repetitive peaks, albeit not as prominent as the cold-start POA possibly due to the lower signal. These
270 results suggest that the lower global in-cylinder temperatures in PCCI compared to CDC (50) resulted in a portion of
271 the emissions experiencing temperature histories (550 K – 750 K) conducive to the formation of first-stage POA
272 (OxyPOA). Previous studies have reported substantial increase in emissions of POA relative to mature soot for
273 various ACI strategies (51, 52). Our results indicate that a fraction of this POA is OxyPOA.

Discussion

276 The discovery of OxyPOA reported in this study can help solve a long-standing mystery associated with air-quality
277 models persistently predicting lower SOA levels in urban regions compared to observations (53-56). SOA formation
278 in air quality models is simulated based on parameterizations derived from smog-chamber experiments that involve
279 oxidizing SOA precursors found in the emissions of various sources, including vehicle emissions. Several culprits
280 have been proposed as possible explanations for the underestimation of SOA formation in these parameterizations,
281 including missing precursors (53) and underestimation of SOA yields of precursors in vehicle emissions (57).
282 Intermediate-volatility organic compounds (IVOCs) and semi-volatile organic compounds (SVOCs) in vehicle
283 emissions, which have particularly high SOA yields, have been hypothesized to be among the missing SOA
284 precursors (58). However, a recent modeling study concluded that accounting for IVOCs and SVOCs played a minor
285 role in closing the gap between modeled and measured SOA over urban areas in southern California (56). Another
286 proposed explanation is vapor wall-loss artifacts in smog chamber experiments leading to underestimation of SOA
287 yields in the derived parameterizations (55, 56). We provide an alternative explanation: the gap between modeled and
288 measured SOA in urban atmospheres is partly due to overestimation of SOA in atmospheric observations, rather than
289 underestimation in models. Atmospheric measurements equate POA from vehicle emissions to HOA and SOA to
290 OOA. However, our results suggest that OxyPOA constitutes a substantial fraction of urban POA emitted from
291 gasoline vehicles during cold-start. Consequently, OxyPOA would be counted as OOA and misattributed to SOA in
292 atmospheric measurements, leading to overestimation of SOA.
293 Quantifying the levels of OxyPOA in urban atmospheres, however, requires further investigation. On the atmospheric
294 measurements front, this entails identifying molecular markers and/or factors that distinguish OxyPOA from
295 anthropogenic SOA. Representing OxyPOA in air-quality models requires incorporating it as a separate POA
296 category alongside traditional POA in vehicle emission inventories. This, in turn, requires performing measurements
297 to quantify emission factors of OxyPOA that take into account variables such as emission certification standards,
298 driving conditions, fuel blends, among others.
299 The detection of OxyPOA in the emissions of the PCCI engine (Fig. 1) suggest a relative increase in OOA compared
300 to HOA in future urban atmospheres if these next-generation ACI strategies are widely adopted. Importantly,
301 quantifying OxyPOA in ACI engine emissions is critical for obtaining a comprehensive understanding of their
302 emission profiles in order to devise control strategies that aid in the development of clean, sustainable transportation
303 energy technologies (59).

Materials and Methods

306 **n-Pentane and n-heptane controlled combustion experiments**
307 The setup used to generate first-stage and second-stage primary organic aerosol (POA) from the controlled
308 combustion of n-pentane and n-heptane is shown in fig. S8 and is described in detail in previous studies (13, 16, 60-
309 62). Briefly, fuel oxidation was temperature-initiated in a 0.24 L custom-built cylindrical quartz chamber enclosed in
310 an insulated heater (Thermcraft Inc., NC, USA). Temperature was controlled to within 1 K using a PID controller
311 (OMEGA, CNi3244) utilizing a high-temperature K-type thermocouple located at the center of the chamber. Fuel
312 was introduced via a bubbler system using a mass flow controller (DAKOTA, 6AGC1AL55-09AB) to direct a stream
313 of ultra-high purity N_2 (NI UHP300, Airgas) into a bubbler containing the fuel. The bubbler dimensions were
314 designed to ensure that the N_2 stream was fully saturated with the fuel vapor at the exit of the bubbler, as verified by
315 mass transfer calculations confirming that the residence time of a bubble rising in the bubbler is greater than the time
316 required to saturate it with the fuel vapor (61). This allowed us to calculate the flowrate of the fuel entering the
317 combustion chamber based on the fuel saturation pressure and N_2 flowrate. The fuel-saturated N_2 stream was then
318 mixed with a controlled stream of clean dry air and N_2 to maintain an equivalence ratio (φ) of 2.3 and O_2/N_2 of 0.06.

319   The total flowrate into the combustion chamber was 0.75 SLPM, resulting in average residence time of
320   approximately 19 seconds. The combustion emissions were then diluted in a 4 L glass dilution chamber with 12
321   SLPM of clean dry air prior to POA sampling. To observe first-stage and second-stage POA formation, the
322   temperature of the combustion chamber was varied between 500 K and 1300 K and the size distributions of the POA
323   emissions were continuously monitored at 90-second time resolution using a scanning mobility particle sizer (SMPS,
324   TSI model 3088). The size distributions were integrated using a particle effective density of 1.3 g/cm^3, estimated
325   using tandem differential mobility analyzer – aerosol particle mass analyzer (tandem DMA-APM) technique (*13, 63*),
326   to obtain temperature-dependent POA mass concentration profiles. As shown in fig. S1, both *n*-pentane and *n*-
327   heptane exhibited two-stage aerosol formation. The first-stage POA peak emission was at 583 K and 563 K for *n*-
328   pentane and *n*-heptane, respectively.
329   We collected POA samples on 47 mm polytetrafluoroethylene (PTFE) filters (0.2 μm pore size, Whatman) for the
330   chemical analyses described below. The collection flowrate was 5 SLPM and the targeted mass loading was 300 μg
331   in order to avoid filter clogging which occurs at ~350 μg. Filters were stored at -15° C pending analysis. First-stage
332   POA samples were collected at combustion temperature of 583 K and 563 K for *n*-pentane and *n*-heptane,
333   respectively. Second-stage POA samples were collected at combustion temperature of 1123 K and 1308 K for *n*-
334   pentane and *n*-heptane, respectively.
335   We also collected samples from *n*-pentane combustion for gas-phase chemical analysis (described below) using a 1-
336   gallon (3.8 L) stainless steel double ended sample cylinder (304L-HDF4-1GAL, Swagelok) fitted with ¼ inch needle
337   valves on both ends (fig. S8). The combustion emissions were sampled directly into the cylinder from the combustion
338   chamber (without dilution) at a flowrate of 0.5 SLPM, and the valves at the inlet and outlet of the cylinder were
339   closed once steady state conditions were achieved. The POA was removed from the emissions using a PTFE filter
340   prior to entering the cylinder. In order to compare the temperature-dependent concentration profiles of gas-phase
341   species emitted during first-stage combustion to that of first-stage POA, we collected gas-phase samples at five
342   temperature points: 543 K, 563 K, 598 K, 658 K, and 743 K. The second-stage gas-phase samples were collected at
343   1143 K.

344   **Cold-start spark-ignition engine experiments**
345   A single cylinder version of a GM LNF 2.0L direct-injected (DI) spark-ignited (SI) 4-cylinder engine was used for
346   these experiments, wherein 3 of the cylinders were disabled by grinding off the cam lobes to prevent valve actuation
347   as well as by drilling holes in the pistons to prevent compression. More details of the engine setup, instrumentation,
348   and cold-start operation are available in previous studies on this engine (*64, 65*). Briefly, the firing cylinder was
349   maintained in stock configuration, wherein the compression ratio, combustion chamber geometry, fuel injector, cam
350   lobe profiles, and cam phasing capabilities were all stock. The engine was fueled with a 9-component surrogate fuel
351   blend known as PACE20 that was designed by the Partnership to Advance Combustion Engines (PACE) consortium
352   to closely mimic the fuel properties such as boiling range and octane rating, as well as engine emissions parameters
353   such as sooting propensity of a market-representative 87 anti-knock index (AKI) E10 fuel while eliminating fuel
354   composition uncertainties from chemical-kinetics modeling. The fuel composition and properties are detailed
355   elsewhere (*65*). Cold-start operation was simulated by operating the engine at 1300 RPM and 2 bar net indicated
356   mean effective pressure (NIMEP) stoichiometric operation while the engine out coolant and oil temperature were
357   controlled to 20°C. For this study, spark timing was used as the engine control parameter to study engine emissions
358   under normal and cold-start conditions. For the data presented in this study, the spark timing was fixed at 25 degrees
359   after-top-dead-center-firing (dATDCf) and the exhaust gas was sampled 35mm downstream of the exhaust port.

360   **Compression-ignition engine experiments**
361   The conventional diesel combustion (CDC) and a premixed charge compression ignition (PCCI) samples were
362   collected from the exhaust of a single-cylinder medium-duty diesel engine. A complete description of the engine and
363   mode operation has been previously described (*66*). Briefly, a 6.7 L Cummins 6-cylinder ISB engine was modified to
364   single cylinder operation by deactivating 5 cylinders and run for these samples on certified ultra-low-sulfur diesel no.
365   ULSD #2 fuel. The same engine was operated in both the CDC and PCCI modes to collect filters samples of aerosol
366   emissions. A similar dilution tunnel set-up as that described for the cold-start experiments was used to collect aerosol
367   samples on PTFE filters. Both samples were collected at 1200 rpm but the PCCI samples was at low load (1.8 bar)
368   and the CDC sample was at high load (3.2 bar) (*67*).

369   **POA chemical analysis using laser desorption ionization mass spectrometry**
370   The POA samples shown in Fig. 1 were analyzed using laser desorption ionization mass spectrometry (LDI-MS) at
371   the University of Georgia proteomics and mass spectrometry core facility. LDI-MS is efficient at detecting incipient
372   soot and has been extensively employed to study soot formation from various combustion sources (*17, 68, 69*). We
373   extracted the POA filter samples by sonicating in 2 ml of dichloromethane (DCM) for 40 minutes. The solutions were
374   then concentrated to 1 ml by evaporation using a gentle stream of ultra-high purity N2. The solutions were then
375   spotted onto a stainless-steel grid for LDI-MS analysis in 250 μL batches, allowing the DCM to evaporate after each
376   batch. Based on our experience (*13, 16, 27*) and in concordance with previous studies (*23, 69-71*), we chose DCM as

377 a solvent for LDI-MS analysis due to its efficacy at extracting large-molecular-size polycyclic aromatic hydrocarbons
378 (PAHs) that constitute incipient soot. LDI-MS analysis was performed on a Bruker Autoflex III in reflectron mode
379 using AutoXecute. Calibration was performed using 2,5 dihydroxybenzoic acid (MH+ = 255.0 m/z; monoisotopic
380 mass), reserpine (609.3 m/z; monoisotopic mass), angiotensin (MH+ = 1296.7 m/z; monoisotopic mass), and insulin
381 (5734.5 m/z; average mass). The instrument uses a 337 nm Nitrogen laser in positive mode. The ion source was set to
382 19 kV and the reflector voltage to 20 kV. Random walk with the raster was set to 2 shots per spot with a total of 100
383 laser shots. The samples were analyzed within two molecular size ranges, 100-1000 m/z and 1000-2000 m/z. The
384 instrument sensitivity was set just below saturating the largest signal within each range in order to detect the large-
385 molecular-size PAHs (Fig. 1A), which would otherwise go undetected if the same sensitivity were applied for the full
386 range (100-2000 m/z).

387 **POA chemical analysis using electrospray ionization mass spectrometry**
388 The POA samples shown in Fig. 1 were analyzed using electrospray ionization Fourier-transform ion cyclotron
389 resonance mass spectrometry (ESI-FTIRC-MS) at the University of Georgia proteomics and mass spectrometry core
390 facility. ESI-MS is efficient at detecting relatively polar molecules (*72-74*) and has been previously employed to
391 perform chemical analysis on various types of organic aerosol (OA) samples, including biomass-burning OA (*74-76*),
392 secondary OA (SOA) (*77-79*), and urban OA (*80, 81*).
393 For ESI-FTIRC-MS analysis, the POA filters were extracted using the same procedure described above for LDI-MS
394 analysis, but using acetonitrile as a solvent because of its efficacy at extracting polar compounds (*79, 82, 83*). An
395 extraction blank with a clean PTFE filter was also prepared following the same steps and was used for background
396 correction. Analysis was performed on a Bruker SolariX 12T FTICR mass spectrometer (Bruker Daltonik, GmbH,
397 Bremen, Germany) in negative ion mode. Mass spectra were collected between 75-1000 m/z with 2M data points
398 length and a 0.4194 second transient. Time of flight was set at 0.8 ms. Samples were infused at a rate of 2.0 µL/min.
399 The capillary voltage was set to 4500 V with a -800 V end plate offset. The nebulizer gas was set to 0.5 bar, and the
400 dry gas was set to 4.0 L/min with a dry temperature of 200° C. Ion accumulation time was 0.005 seconds. Calibration
401 was performed with sodium trifluoroacetate (Sigma-Aldrich) (0.1 mg/mL in 50:50 methanol:water). Spectra were
402 collected in triplicate by doing three injections of 10 µL of sample. Prior to introducing samples to the instrument,
403 methanol and extraction blanks were acquired.
404 For data analysis, 48 scans per injection per sample were averaged using Bruker Compass Data Analysis software
405 (Version 5.3). Background subtraction was performed using Xpose mode with a retention time window of 0.0083s
406 and a ratio of 5 in order to minimize noise signals and signals that were detected in the extraction blanks. MFAssignR
407 (*84*), an open source R package, was used to analyze the data according to component molecular formulae.
408 Assignments were internally recalibrated, and subjected to the following restrictions: CxHyOz, $0.3 \leq H/C \leq 3$, $0 \leq$
409 $O/C \leq 2.5$, and a maximum allowable error ≤ 1 ppm. The final peak list that represents each sample is composed of
410 molecular formulae that are common across the three injections. The number of molecular assignments was 1014 for
411 *n*-pentane first-stage POA, 1525 for *n*-heptane first-stage POA, 206 for the cold-start spark-ignition engine POA, and
412 185 for the PCCI engine POA. The *n*-pentane second-stage POA, *n*-heptane second-stage POA, and CDC POA had
413 no signal. Average O/C values shown in Fig. 1C were calculated as signal-weighted averages of O/C values of the
414 individual molecules identified in the ESI-MS spectra.

415 **POA chemical analysis using nanospray desorption electrospray ionization mass spectrometry**
416 In addition to ESI-FTIRC-MS, the *n*-heptane first-stage POA was also analyzed at the Pacific Northwest National
417 Laboratory (PNNL) Environmental Molecular Sciences Laboratory (EMSL) using nanospray desorption electrospray
418 ionization (nano-DESI) high resolution mass spectrometry.
419 The design of the nano-DESI high resolution mass spectrometry (HRMS) interface has been previously described in
420 (*85, 86*). Briefly, a 7/3 v/v acetonitrile/water solvent mixture (Optima LC-MS grade; Fisher Chemical, Hampton
421 USA) was flowed at 0.5 µL/min through a capillary assembly formed by two fused silica capillaries aligned at ~90°
422 (Polymicro Technologies, Phoenix, USA; primary capillary: 150 µm O.D., 50 µm I.D.; secondary capillary: 150 µm
423 O.D., 20 µm I.D. with etched terminus (*87*)). This junction was brought sufficiently close to the PTFE filter samples
424 such that a liquid junction formed and scanned along the XY plane at 35 µm/s, allowing for continuous and direct
425 sampling from the filters. -3.5 kV was applied via the solvent syringe needle, and the nano-DESI capillary assembly
426 was positioned ~1 mm from the inlet of a high-resolution LTQ Velos Orbitrap mass spectrometer (Thermo Scientific,
427 Waltham). The MS inlet was maintained at 275°C. All samples were analyzed in negative ion mode via MS1 (m/z
428 100 – 1000) with an automatic gain control (AGC) target of 5 x 105, maximum ion injection time of 500 ms, and
429 mass resolution of 100k at m/z 400.
430 For data analysis, 100 scans were averaged per sample within Xcalibur (Thermo Scientific) and exported as a .csv
431 peak list (5 decimal points per m/z). MFAssignR was used for component molecular formulae assignment. For
432 features with S/N > 6, assignments were internally recalibrated, and subjected to the following restrictions: CxHyOz;
433 $0.3 \leq H/C \leq 3$; $O/C \leq 2.5$; $-20 \leq DBE-O \leq 25$ (DBE-O: double bond equivalents minus oxygen count). Datasets were
434 blank subtracted such that molecular formulae detected in both a solvent blank and sample list were removed from
435 the final sample list if they were present in the sample at 3x or lower the level found in the blank. Final datasets were

436 manually inspected/cleaned for outlier assignments (*86*). The final peak list used in the interpretations for each
437 sample is composed of only molecular formulae commonly detected across each of three replicates. The number of
438 molecular assignments was 1895 for *n*-heptane first-stage POA.

439 **Gas-phase chemical analysis using electron-impact mass spectrometry and vacuum ultraviolet absorption spectroscopy**
440 Using a filtration system to remove particles, gas-phase samples were collected for offline analysis from the
441 controlled combustion of *n*-pentane. In order to compare the temperature-dependent concentration profiles of gas-
442 phase species emitted during first-stage combustion to that of first-stage POA, we collected gas-phase samples at five
443 temperature points: 543 K, 563 K, 598 K, 658 K, and 743 K. The second-stage samples were collected at 1143 K.
444 Gas-phase samples were compressed in an inert-coated chamber and then introduced into a valving system connected
445 to a gas chromatograph (GC), which collects 500 μL of the sample. The 500-μL volume was then introduced via the
446 GC to three different detectors. First, the sample was directed through a 5Å molecular-sieve which separates CO,
447 CO_2, H_2, O_2, and CH_4, for analysis via a thermal conductivity detector (TCD) using Ar as reference gas. The filtered
448 sample was then split into two volumes of 250 μL which are injected sequentially onto two identical PONA columns
449 of 100 m length, 250 μm inner diameter, and 0.50 μm film thickness. The two columns follow the same temperature
450 programming which begins with holding at 40 °C for 5 minutes, increasing to 110 °C at 5 °C/min, holding at 110 °C
451 for 5 minutes, increasing to 280 °C at 5 °C/min, and holding at 280 °C for 5 minutes.
452 One PONA column leads to a 70-eV electron-impact mass-spectrometer (EI-MS), while the other leads to a vacuum-
453 ultraviolet (VUV) absorption cell which is held at 50 °C and 795 ± 2 torr. Species quantification was achieved
454 through fitting of measured absorption spectra to reference spectra at photon energies with high signal-to-noise ratios
455 lying within the full-scale range of 5.17 – 9.92 eV. Prior to quantification, reference spectra were created from
456 injection of reference gas samples, typically at 1000 ppm. VUV spectra of the detected species are shown in fig. S9-
457 S17.

458 **Gas-particle partitioning perturbation experiments**
459 In order to assess the effect of oligomer dissociation on the evaporation behavior of OxyPOA, we subjected the
460 OxyPOA emissions from *n*-pentane combustion to two perturbations: (i) dilution with clean air at room temperature,
461 and (ii) heating in a thermodenuder at temperatures ranging between 303 K and 363 K. Both dilution and heating
462 perturb the gas-particle equilibrium partitioning and force the particles to evaporate in order to reestablish
463 equilibrium. If the particle phase contains oligomers, the perturbation induces not only physical evaporation (i.e.
464 partitioning of molecules from the particle phase to the gas phase), but also oligomer dissociation (*47*). The reason is
465 that monomers evaporate more readily than the oligomers due to their smaller molecular size, thus higher volatility.
466 This perturbs the monomer-oligomer equilibrium in the particle phase, leading to oligomer dissociation to reestablish
467 equilibrium. Quantifying the equilibrium composition of monomers and oligomers is not straightforward. However,
468 the dissociation rate constant is known to increase substantially more than the association rate constant with increase
469 in temperature (*47*). In other words, the monomer-oligomer equilibrium composition shifts toward higher fraction of
470 monomers as temperature increases, making the aerosol more volatile because monomers are more volatile than
471 oligomers. Consequently, the effect of oligomer dissociation would be more prominent if the aerosol is heated in a
472 thermodenuder compared to dilution at room temperature. Here, we probe this temperature-dependent oligomer
473 dissociation effect by comparing the apparent volatility of the OxyPOA, namely saturation concentration (C_{sat}),
474 needed to explain the extent of evaporation in the dilution versus thermodenuder perturbations. If higher C_{sat} values
475 are required to reproduce the observed evaporation in the thermodenuder measurements compared to dilution, this
476 would be evidence that the OxyPOA contains oligomers.
477 In both the dilution and thermodenuder experiments, the combustion chamber temperature was set to 583 K,
478 corresponding to the peak OxyPOA emissions (fig. S1). The thermodenuder experiments involved diluting the
479 combustion emissions (0.75 SLPM) with 12 SLPM of clean air and then alternating between measuring the baseline
480 aerosol mass concentration at room temperature ($C_{OA,0}$) by sampling through the bypass and measuring the aerosol
481 mass concentration (C_{OA}) at 303 K, 323 K, 343 K, and 363 K by sampling through the thermodenuder (fig. S8). The
482 thermodenuder consisted of a stainless-steel tube wrapped with heating tape and insulation. The temperature was
483 controlled using a PID controller (OMEGA, CNi3244). The thermodenuder has a volume of 0.5 L (diameter = 2.54
484 cm, length = 1 m) and the aerosol flow was 1 SLPM, yielding an average residence time of 30 seconds. In the
485 dilution experiments, we first obtained a baseline aerosol mass concentration ($C_{OA,0}$) by mixing the combustion
486 emissions (0.75 SLPM) with 3 SLPM of clean air in the dilution chamber (fig. S8). We then applied three dilution
487 factors (DFs) of approximately 5, 8, and 10, and measured the aerosol mass concentration (C_{OA}) at each DF. The
488 aerosol emissions in the dilution experiment were also sampled through the thermodenuder, but without heating, to
489 allow for ample time for evaporation.
490 We performed gas-particle equilibrium calculations (*88*) to interpret the observed OxyPOA evaporation at the
491 dilution and thermodenuder experimental conditions. We first calculated the reference saturation concentration at 300
492 K ($C_{sat,ref}$) of the each of the assigned molecules (see above for molecular assignments) based on the parameterization
493 of Li *et al.* (*89*):

---

494 $$\log_{10}(C_{\text{sat,ref}}) = (n_C^0 - n_C)\, b_C - n_O\, b_O - 2\, \frac{n_C\, n_O}{n_C + n_O}\, b_{CO} \tag{1}$$

495 Where, n_C is the number of carbon atoms, n_O is the number of oxygen atoms, $n_C^0 = 22.6$, $b_C = 0.4481$, $b_O = 1.656$,
496 and $b_{CO} = -0.779$.
497 The molecules were then grouped into five volatility bins that correspond to:
498   1. Intermediate-volatility organic compounds (IVOCs): $C_{\text{sat,ref}} > 300$ µg/m^3.
499   2. Semi-volatile organic compounds (SVOCs): 0.3 µg/m$^3 < C_{\text{sat,ref}} < 300$ µg/m^3.
500   3. Low-volatility organic compounds (LVOCs): 3×10^{-4} µg/m$^3 < C_{\text{sat,ref}} < 0.3$ µg/m^3.
501   4. Extremely low volatility organic compounds (ELVOCs): 3×10^{-9} µg/m$^3 < C_{\text{sat,ref}} < 3 \times 10^{-4}$ µg/m^3.
502   5. Ultra-low volatility organic compounds (ULVOCs): $C_{\text{sat,ref}} < 3 \times 10^{-9}$ µg/m^3.
503 We then assigned $C_{\text{sat,ref}}$ value for each bin, calculated as the average $C_{\text{sat,ref}}$ of the components in the bin. We
504 calculated C_{sat} values at different temperatures ($C_{\text{sat}}(T)$) using the Clausius-Clapeyron relation:

505 $$C_{\text{sat}}(T) = C_{\text{sat,ref}} \frac{T_{\text{ref}}}{T} \exp\left(\frac{-\Delta H}{R}\left(\frac{1}{T} - \frac{1}{T_{\text{ref}}}\right)\right) \tag{2}$$

506 Where, T_{ref} is the reference temperature (300 K), R is the universal gas constant, and ΔH is the enthalpy of
507 vaporization, estimated using the parameterization of Epstein $et\ al.$ (90):
508 $$\Delta H \text{ [kJ/mol]} = -11 \log_{10}(C_{\text{sat,ref}}) + 129 \tag{3}$$
509 We then employed an iterative solution to calculate C_{OA} at each experimental condition (for both dilution and
510 thermodenuder experiments) following Donahue $et\ al.$ (88):

511 $$z_i = \left(1 + \frac{C_{\text{sat,i}}}{C_{OA}}\right)^{-1}; \ C_{OA} = \sum_i C_i\, z_i \tag{4}$$

512 Where, the subscript 'i' refers to a specific volatility bin, z is the portioning coefficient between the particle phase and
513 the gas phase, and C is the total concentration in both phases.
514 The equilibrium-partitioning C_{OA} values calculated using the volatility distribution obtained from molecular
515 assignments correspond to the black lines in Fig. 4A and Fig. 4C. We also obtained a volatility distribution that yields
516 equilibrium-partitioning C_{OA} values that fit the thermodenuder measurements by adjusting the mass fractions in the
517 volatility bins. These equilibrium-partitioning C_{OA} values correspond to the brown lines in Fig. 4A and Fig. 4C.
518
519

520 # References
521 1.   D. W. Dockery, C. A. Pope, X. Xu, J. D. Spengler, J. H. Ware, M. E. Fay, B. G. Ferris Jr, F. E. Speizer, An
522   association between air pollution and mortality in six US cities. *New England journal of medicine* **329**, 1753-
523   1759 (1993).
524 2.   T. Pervin, U.-G. Gerdtham, C. H. Lyttkens, Societal costs of air pollution-related health hazards: A review of
525   methods and results. *Cost Effectiveness and Resource Allocation* **6**, 1-22 (2008).
526 3.   D. C. R. H.-O. Pörtner, M. Tignor, E.S. Poloczanska, K. Mintenbeck, A. Alegría, M. Craig, S. Langsdorf, S.
527   Löschke, V. Möller, A. Okem, B. Rama (eds.), "IPCC, 2022: Climate Change 2022: Impacts, Adaptation, and
528   Vulnerability. Contribution of Working Group II to the Sixth Assessment Report of the Intergovernmental
529   Panel on Climate Change," (2022).
530 4.   J. L. Jimenez, M. Canagaratna, N. Donahue, A. Prevot, Q. Zhang, J. H. Kroll, P. F. DeCarlo, J. D. Allan, H.
531   Coe, N. Ng, Evolution of organic aerosols in the atmosphere. *science* **326**, 1525-1529 (2009).
532 5.   K. Johansson, M. Head-Gordon, P. Schrader, K. Wilson, H. Michelsen, Resonance-stabilized hydrocarbon-
533   radical chain reactions may explain soot inception and growth. *Science* **361**, 997-1000 (2018).
534 6.   O. Welz, J. D. Savee, D. L. Osborn, S. S. Vasu, C. J. Percival, D. E. Shallcross, C. A. Taatjes, Direct kinetic
535   measurements of Criegee intermediate (CH2OO) formed by reaction of CH2I with O2. *Science* **335**, 204-207
536   (2012).
537 7.   C. A. Taatjes, O. Welz, A. J. Eskola, J. D. Savee, A. M. Scheer, D. E. Shallcross, B. Rotavera, E. P. Lee, J.
538   M. Dyke, D. K. Mok, Direct measurements of conformer-dependent reactivity of the Criegee intermediate
539   CH3CHOO. *Science* **340**, 177-180 (2013).
540 8.   Q. Zhang, J. L. Jimenez, M. Canagaratna, J. D. Allan, H. Coe, I. Ulbrich, M. Alfarra, A. Takami, A.
541   Middlebrook, Y. Sun, Ubiquity and dominance of oxygenated species in organic aerosols in
542   anthropogenically-influenced Northern Hemisphere midlatitudes. *Geophysical research letters* **34**, (2007).
543 9.   I. Ulbrich, M. Canagaratna, Q. Zhang, D. Worsnop, J. Jimenez, Interpretation of organic components from
544   Positive Matrix Factorization of aerosol mass spectrometric data. *Atmospheric Chemistry and Physics* **9**, 2891-
545   2918 (2009).
546 10.   J. D. Savee, E. Papajak, B. Rotavera, H. Huang, A. J. Eskola, O. Welz, L. Sheps, C. A. Taatjes, J. Zádor, D.
547   L. Osborn, Direct observation and kinetics of a hydroperoxyalkyl radical (QOOH). *Science* **347**, 643-646
548   (2015).

549　11.　A. S. Hansen, T. Bhagde, K. B. Moore III, D. R. Moberg, A. W. Jasper, Y. Georgievskii, M. F. Vansco, S. J.
550　　　　Klippenstein, M. I. Lester, Watching a hydroperoxyalkyl radical (• QOOH) dissociate. *Science* **373**, 679-682
551　　　　(2021).

552　12.　B. Rotavera, C. A. Taatjes, Influence of functional groups on low-temperature combustion chemistry of
553　　　　biofuels. *Progress in Energy and Combustion Science* **86**, 100925 (2021).

554　13.　O. El Hajj, K. Atwi, Z. Cheng, A. Koritzke, M. Christianson, N. Dewey, B. Rotavera, R. Saleh, Two-stage
555　　　　aerosol formation in low-temperature combustion. *Fuel* **304**, 121322 (2021).

556　14.　H. Michelsen, Probing soot formation, chemical and physical evolution, and oxidation: A review of in situ
557　　　　diagnostic techniques and needs. *Proceedings of the Combustion Institute* **36**, 717-735 (2017).

558　15.　T. C. Bond, S. J. Doherty, D. W. Fahey, P. M. Forster, T. Berntsen, B. J. DeAngelo, M. G. Flanner, S. Ghan,
559　　　　B. Kärcher, D. Koch, Bounding the role of black carbon in the climate system: A scientific assessment. *Journal*
560　　　　*of Geophysical Research: Atmospheres* **118**, 5380-5552 (2013).

561　16.　R. Saleh, Z. Cheng, K. Atwi, The brown–black continuum of light-absorbing combustion aerosols.
562　　　　*Environmental Science & Technology Letters* **5**, 508-513 (2018).

563　17.　A. Faccinetto, C. Focsa, P. Desgroux, M. Ziskind, Progress toward the quantitative analysis of PAHs adsorbed
564　　　　on soot by laser desorption/laser ionization/time-of-flight mass spectrometry. *Environmental science &*
565　　　　*technology* **49**, 10510-10520 (2015).

566　18.　Y. Ju, Understanding cool flames and warm flames. *Proceedings of the Combustion Institute* **38**, 83-119
567　　　　(2021).

568　19.　H. Zhao, L. Wu, C. Patrick, Z. Zhang, Y. Rezgui, X. Yang, G. Wysocki, Y. Ju, Studies of low temperature
569　　　　oxidation of n-pentane with nitric oxide addition in a jet stirred reactor. *Combustion and Flame* **197**, 78-87
570　　　　(2018).

571　20.　R. W. Wheeler, D. Downs, A. D. Walsh, 'Knock' in Internal Combustion Engines. *Nature* **162**, 893-894 (1948).

572　21.　C. K. Westbrook, M. Mehl, W. J. Pitz, G. Kukkadapu, S. Wagnon, K. Zhang, Multi-fuel surrogate chemical
573　　　　kinetic mechanisms for real world applications. *Physical Chemistry Chemical Physics* **20**, 10588-10606
574　　　　(2018).

575　22.　J. Zádor, C. A. Taatjes, R. X. Fernandes, Kinetics of elementary reactions in low-temperature autoignition
576　　　　chemistry. *Progress in energy and combustion science* **37**, 371-421 (2011).

577　23.　A. Michela, A. Barbara, T. Antonio, C. Anna, Identification of large polycyclic aromatic hydrocarbons in
578　　　　carbon particulates formed in a fuel-rich premixed ethylene flame. *Carbon* **46**, 2059-2066 (2008).

579　24.　B. Apicella, M. Millan, A. Herod, A. Carpentieri, P. Pucci, A. Ciajolo, Separation and measurement of flame-
580　　　　formed high molecular weight polycyclic aromatic hydrocarbons by size-exclusion chromatography and laser
581　　　　desorption/ionization time-of-flight mass spectrometry. *Rapid Communications in Mass Spectrometry: An*
582　　　　*International Journal Devoted to the Rapid Dissemination of Up-to-the-Minute Research in Mass*
583　　　　*Spectrometry* **20**, 1104-1108 (2006).

584　25.　J. A. Rundel, C. M. Thomas, P. E. Schrader, K. R. Wilson, K. O. Johansson, R. P. Bambha, H. A. Michelsen,
585　　　　Promotion of particle formation by resonance-stabilized radicals during hydrocarbon pyrolysis. *Combustion*
586　　　　*and Flame* **243**, 111942 (2022).

587　26.　J. A. Rundel, K. O. Johansson, P. E. Schrader, R. P. Bambha, K. R. Wilson, J. Zádor, G. B. Ellison, H. A.
588　　　　Michelsen, Production of aliphatic-linked polycyclic hydrocarbons during radical-driven particle formation
589　　　　from propyne and propene pyrolysis. *Combustion and Flame*, 112457 (2022).

590　27.　K. Atwi, A. Mondal, J. Pant, Z. Cheng, O. El Hajj, I. Ijeli, H. Handa, R. Saleh, Physicochemical properties
591　　　　and cytotoxicity of brown carbon produced under different combustion conditions. *Atmospheric Environment*
592　　　　**244**, 117881 (2021).

593　28.　M. Canagaratna, J. Jimenez, J. Kroll, Q. Chen, S. Kessler, P. Massoli, L. Hildebrandt Ruiz, E. Fortner, L.
594　　　　Williams, K. Wilson, Elemental ratio measurements of organic compounds using aerosol mass spectrometry:
595　　　　characterization, improved calibration, and implications. *Atmospheric Chemistry and Physics* **15**, 253-272
596　　　　(2015).

597　29.　F. Mahrt, E. Newman, Y. Huang, M. Ammann, A. K. Bertram, Phase Behavior of Hydrocarbon-like Primary
598　　　　Organic Aerosol and Secondary Organic Aerosol Proxies Based on Their Elemental Oxygen-to-Carbon Ratio.
599　　　　*Environmental Science & Technology* **55**, 12202-12214 (2021).

600　30.　M. Kalberer, D. Paulsen, M. Sax, M. Steinbacher, J. Dommen, A. S. Prévôt, R. Fisseha, E. Weingartner, V.
601　　　　Frankevich, R. Zenobi, Identification of polymers as major components of atmospheric organic aerosols.
602　　　　*Science* **303**, 1659-1662 (2004).

603　31.　W. A. Hall IV, M. V. Johnston, Oligomer formation pathways in secondary organic aerosol from MS and
604　　　　MS/MS measurements with high mass accuracy and resolving power. *Journal of the American Society for*
605　　　　*Mass Spectrometry* **23**, 1097-1108 (2012).

606　32.　M. P. Tolocka, M. Jang, J. M. Ginter, F. J. Cox, R. M. Kamens, M. V. Johnston, Formation of oligomers in
607　　　　secondary organic aerosol. *Environmental Science & Technology* **38**, 1428-1434 (2004).

33. H. K. Maben, P. J. Ziemann, Kinetics of oligomer-forming reactions involving the major functional groups present in atmospheric secondary organic aerosol particles. *Environmental Science: Processes & Impacts*, (2023).

34. M. K. Shrivastava, T. E. Lane, N. M. Donahue, S. N. Pandis, A. L. Robinson, Effects of gas particle partitioning and aging of primary emissions on urban and regional organic aerosol concentrations. *Journal of Geophysical Research: Atmospheres* **113**, (2008).

35. S. H. Budisulistiorini, J. Chen, M. Itoh, M. Kuwata, Can Online Aerosol Mass Spectrometry Analysis Classify Secondary Organic Aerosol (SOA) and Oxidized Primary Organic Aerosol (OPOA)? A Case Study of Laboratory and Field Studies of Indonesian Biomass Burning. *ACS Earth and Space Chemistry* **5**, 3511-3522 (2021).

36. M. Frenklach, H. Wang, in *Symposium (International) on Combustion*. (Elsevier, 1991), vol. 23, pp. 1559-1566.

37. K. O. Johansson, T. Dillstrom, M. Monti, F. El Gabaly, M. F. Campbell, P. E. Schrader, D. M. Popolan-Vaida, N. K. Richards-Henderson, K. R. Wilson, A. Violi, Formation and emission of large furans and oxygenated hydrocarbons from flames. *Proceedings of the National Academy of Sciences* **113**, 8374-8379 (2016).

38. J. Bugler, A. Rodriguez, O. Herbinet, F. Battin-Leclerc, C. Togbé, G. Dayma, P. Dagaut, H. J. Curran, An experimental and modelling study of n-pentane oxidation in two jet-stirred reactors: The importance of pressure-dependent kinetics and new reaction pathways. *Proceedings of the Combustion Institute* **36**, 441-448 (2017).

39. M. G. Christianson, A. C. Doner, M. M. Davis, A. L. Koritzke, J. M. Turney, H. F. Schaefer III, L. Sheps, D. L. Osborn, C. A. Taatjes, B. Rotavera, Reaction mechanisms of a cyclic ether intermediate: Ethyloxirane. *International Journal of Chemical Kinetics* **53**, 43-59 (2021).

40. A. C. Doner, M. M. Davis, A. L. Koritzke, M. G. Christianson, J. M. Turney, H. F. Schaefer III, L. Sheps, D. L. Osborn, C. A. Taatjes, B. Rotavera, Isomer-dependent reaction mechanisms of cyclic ether intermediates: cis-2, 3-dimethyloxirane and trans-2, 3-dimethyloxirane. *International journal of chemical kinetics* **53**, 127-145 (2021).

41. A. C. Doner, J. Zádor, B. Rotavera, Stereoisomer-dependent unimolecular kinetics of 2, 4-dimethyloxetanyl peroxy radicals. *Faraday Discussions* **238**, 295-319 (2022).

42. A. L. Koritzke, N. S. Dewey, M. G. Christianson, S. Hartness, A. C. Doner, A. R. Webb, B. Rotavera, Probing O2-dependence of tetrahydrofuranyl reactions via isomer-resolved speciation. *Combustion and Flame*, 112640 (2023).

43. F. Bianchi, T. Kurtén, M. Riva, C. Mohr, M. P. Rissanen, P. Roldin, T. Berndt, J. D. Crounse, P. O. Wennberg, T. F. Mentel, Highly oxygenated organic molecules (HOM) from gas-phase autoxidation involving peroxy radicals: A key contributor to atmospheric aerosol. *Chemical reviews* **119**, 3472-3509 (2019).

44. S. W. Hartness, N. S. Dewey, M. G. Christianson, A. L. Koritzke, A. C. Doner, A. R. Webb, B. Rotavera, Probing O2 dependence of hydroperoxy-butyl reactions via isomer-resolved speciation. *Proceedings of the Combustion Institute*, (2022).

45. N. Belhadj, M. Lailliau, R. Benoit, P. Dagaut, Experimental and kinetic modeling study of n-hexane oxidation. Detection of complex low-temperature products using high-resolution mass spectrometry. *Combustion and Flame* **233**, 111581 (2021).

46. N. M. Donahue, S. Epstein, S. N. Pandis, A. L. Robinson, A two-dimensional volatility basis set: 1. organic-aerosol mixing thermodynamics. *Atmospheric Chemistry and Physics* **11**, 3303-3318 (2011).

47. E. Trump, N. Donahue, Oligomer formation within secondary organic aerosols: equilibrium and dynamic considerations. *Atmospheric Chemistry and Physics* **14**, 3691-3701 (2014).

48. D. R. Gentner, S. H. Jathar, T. D. Gordon, R. Bahreini, D. A. Day, I. El Haddad, P. L. Hayes, S. M. Pieber, S. M. Platt, J. de Gouw, Review of urban secondary organic aerosol formation from gasoline and diesel motor vehicle emissions. *Environmental science & technology* **51**, 1074-1093 (2017).

49. M. S. Reiter, K. M. Kockelman, The problem of cold starts: A closer look at mobile source emissions levels. *Transportation Research Part D: Transport and Environment* **43**, 123-132 (2016).

50. A. K. Agarwal, A. P. Singh, R. K. Maurya, Evolution, challenges and path forward for low temperature combustion engines. *Progress in Energy and Combustion Science* **61**, 1-56 (2017).

51. M. Moses-DeBusk, S. J. Curran, S. A. Lewis, R. M. Connatser, J. M. Storey, Impacts of Air-Fuel Stratification in ACI Combustion on Particulate Matter and Gaseous Emissions. *Emission Control Science and Technology* **5**, 225-237 (2019).

52. G. Lucachick, S. Curran, J. Storey, V. Prikhodko, W. F. Northrop, Volatility characterization of nanoparticles from single and dual-fuel low temperature combustion in compression ignition engines. *Aerosol Science and Technology* **50**, 436-447 (2016).

53. R. Volkamer, J. L. Jimenez, F. San Martini, K. Dzepina, Q. Zhang, D. Salcedo, L. T. Molina, D. R. Worsnop, M. J. Molina, Secondary organic aerosol formation from anthropogenic air pollution: Rapid and higher than expected. *Geophysical Research Letters* **33**, (2006).

54. K. S. Docherty, E. A. Stone, I. M. Ulbrich, P. F. DeCarlo, D. C. Snyder, J. J. Schauer, R. E. Peltier, R. J. Weber, S. M. Murphy, J. H. Seinfeld, Apportionment of primary and secondary organic aerosols in Southern California during the 2005 Study of Organic Aerosols in Riverside (SOAR-1). *Environmental science & technology* **42**, 7655-7662 (2008).

55. C. D. Cappa, S. H. Jathar, M. J. Kleeman, K. S. Docherty, J. L. Jimenez, J. H. Seinfeld, A. S. Wexler, Simulating secondary organic aerosol in a regional air quality model using the statistical oxidation model–Part 2: Assessing the influence of vapor wall losses. *Atmospheric Chemistry and Physics* **16**, 3041-3059 (2016).

56. A. Akherati, C. D. Cappa, M. J. Kleeman, K. S. Docherty, J. L. Jimenez, S. M. Griffith, S. Dusanter, P. S. Stevens, S. H. Jathar, Simulating secondary organic aerosol in a regional air quality model using the statistical oxidation model–Part 3: Assessing the influence of semi-volatile and intermediate-volatility organic compounds and NO x. *Atmospheric Chemistry and Physics* **19**, 4561-4594 (2019).

57. J. Ensberg, P. Hayes, J. Jimenez, J. Gilman, W. Kuster, J. De Gouw, J. Holloway, T. Gordon, S. Jathar, A. Robinson, Emission factor ratios, SOA mass yields, and the impact of vehicular emissions on SOA formation. *Atmospheric Chemistry and Physics* **14**, 2383-2397 (2014).

58. Y. Zhao, R. Saleh, G. Saliba, A. A. Presto, T. D. Gordon, G. T. Drozd, A. H. Goldstein, N. M. Donahue, A. L. Robinson, Reducing secondary organic aerosol formation from gasoline vehicle exhaust. *Proceedings of the National Academy of Sciences* **114**, 6984-6989 (2017).

59. K. Kohse-Höinghaus, Combustion, Chemistry, and Carbon Neutrality. *Chemical Reviews* **123**, 5139-5219 (2023).

60. Z. Cheng, K. Atwi, O. E. Hajj, I. Ijeli, D. A. Fischer, G. Smith, R. Saleh, Discrepancies between brown carbon light-absorption properties retrieved from online and offline measurements. *Aerosol Science and Technology*, 1-12 (2020).

61. Z. Cheng, K. Atwi, T. Onyima, R. Saleh, Investigating the dependence of light-absorption properties of combustion carbonaceous aerosols on combustion conditions. *Aerosol Science and Technology* **53**, 419-434 (2019).

62. Z. Cheng, K. M. Atwi, Z. Yu, A. Avery, E. C. Fortner, L. Williams, F. Majluf, J. E. Krechmer, A. T. Lambe, R. Saleh, Evolution of the light-absorption properties of combustion brown carbon aerosols following reaction with nitrate radicals. *Aerosol Science and Technology* **54**, 849-863 (2020).

63. P. H. McMurry, X. Wang, K. Park, K. Ehara, The relationship between mass and mobility for atmospheric particles: A new technique for measuring particle density. *Aerosol Science & Technology* **36**, 227-238 (2002).

64. G. S. Jatana, F. D. F. Chuahy, J. Szybist, The effect of spark-plug heat dispersal range and exhaust valve opening timing on cold-start emissions and cycle-to-cycle variability. *SAE International Journal of Advances and Current Practices in Mobility* **4**, 462-471 (2021).

65. G. S. Jatana, F. D. F. Chuahy, J. Szybist, "Effect of Split-Injection Strategies on Engine Performance and Emissions under Cold-Start Operation," (SAE Technical Paper, 2023).

66. S. Curran, J. Szybist, B. Kaul, J. Easter, S. Sluder, Fuel Stratification Effects on Gasoline Compression Ignition with a Regular-Grade Gasoline on a Single-Cylinder Medium-Duty Diesel Engine at Low Load. *SAE Technical Paper Series* **2021**, (2021).

67. Y. Park, M. Moses-DeBusk, S. S. Sluder, S. P. Huff, Impact of Biofuel Blending on Hydrocarbon Speciation and Particulate Matter from a Medium-Duty Multimode Combustion Strategy. *Energies* **16**, 5735 (2023).

68. A. Faccinetto, P. Desgroux, M. Ziskind, E. Therssen, C. Focsa, High-sensitivity detection of polycyclic aromatic hydrocarbons adsorbed onto soot particles using laser desorption/laser ionization/time-of-flight mass spectrometry: An approach to studying the soot inception process in low-pressure flames. *Combustion and Flame* **158**, 227-239 (2011).

69. B. Apicella, A. Carpentieri, M. Alfè, R. Barbella, A. Tregrossi, P. Pucci, A. Ciajolo, Mass spectrometric analysis of large PAH in a fuel-rich ethylene flame. *Proceedings of the Combustion Institute* **31**, 547-553 (2007).

70. C. Russo, F. Stanzione, A. Ciajolo, A. Tregrossi, Study on the contribution of different molecular weight species to the absorption UV–Visible spectra of flame-formed carbon species. *Proceedings of the Combustion Institute* **34**, 3661-3668 (2013).

71. B. Apicella, C. Russo, A. Carpentieri, A. Tregrossi, A. Ciajolo, PAHs and fullerenes as structural and compositional motifs tracing and distinguishing organic carbon from soot. *Fuel* **309**, 122356 (2022).

72. A. P. Bateman, J. Laskin, A. Laskin, S. A. Nizkorodov, Applications of high-resolution electrospray ionization mass spectrometry to measurements of average oxygen to carbon ratios in secondary organic aerosols. *Environmental science & technology* **46**, 8315-8324 (2012).

73. P. Lin, P. K. Aiona, Y. Li, M. Shiraiwa, J. Laskin, S. A. Nizkorodov, A. Laskin, Molecular characterization of brown carbon in biomass burning aerosol particles. *Environmental science & technology* **50**, 11815-11824 (2016).

74. P. Lin, L. T. Fleming, S. A. Nizkorodov, J. Laskin, A. Laskin, Comprehensive molecular characterization of atmospheric brown carbon by high resolution mass spectrometry with electrospray and atmospheric pressure photoionization. *Analytical chemistry* **90**, 12493-12502 (2018).

75. A. P. Bateman, S. A. Nizkorodov, J. Laskin, A. Laskin, High-resolution electrospray ionization mass spectrometry analysis of water-soluble organic aerosols collected with a particle into liquid sampler. *Analytical chemistry* **82**, 8010-8016 (2010).

76. S. H. Budisulistiorini, M. Riva, M. Williams, J. Chen, M. Itoh, J. D. Surratt, M. Kuwata, Light-absorbing brown carbon aerosol constituents from combustion of Indonesian peat and biomass. *Environmental Science & Technology* **51**, 4415-4423 (2017).

77. C. M. Kenseth, N. J. Hafeman, Y. Huang, N. F. Dalleska, B. M. Stoltz, J. H. Seinfeld, Synthesis of carboxylic acid and dimer ester surrogates to constrain the abundance and distribution of molecular products in α-pinene and β-pinene secondary organic aerosol. *Environmental Science & Technology* **54**, 12829-12839 (2020).

78. R. Zhao, C. M. Kenseth, Y. Huang, N. F. Dalleska, J. H. Seinfeld, Iodometry-assisted liquid chromatography electrospray ionization mass spectrometry for analysis of organic peroxides: An application to atmospheric secondary organic aerosol. *Environmental science & technology* **52**, 2108-2117 (2018).

79. A. P. Bateman, M. L. Walser, Y. Desyaterik, J. Laskin, A. Laskin, S. A. Nizkorodov, The effect of solvent on the analysis of secondary organic aerosol using electrospray ionization mass spectrometry. *Environmental science & technology* **42**, 7341-7346 (2008).

80. M. Teich, D. van Pinxteren, M. Wang, S. Kecorius, Z. Wang, T. Müller, G. Močnik, H. Herrmann, Contributions of nitrated aromatic compounds to the light absorption of water-soluble and particulate brown carbon in different atmospheric environments in Germany and China. *Atmospheric Chemistry and Physics* **17**, 1653-1672 (2017).

81. Z. Kitanovski, I. Grgić, R. Vermeylen, M. Claeys, W. Maenhaut, Liquid chromatography tandem mass spectrometry method for characterization of monoaromatic nitro-compounds in atmospheric particulate matter. *Journal of Chromatography A* **1268**, 35-43 (2012).

82. Y. Cheng, K.-b. He, Z.-y. Du, G. Engling, J.-m. Liu, Y.-l. Ma, M. Zheng, R. J. Weber, The characteristics of brown carbon aerosol during winter in Beijing. *Atmospheric Environment* **127**, 355-364 (2016).

83. J. Liu, M. Bergin, H. Guo, L. King, N. Kotra, E. Edgerton, R. Weber, Size-resolved measurements of brown carbon in water and methanol extracts and estimates of their contribution to ambient fine-particle light absorption. *Atmospheric Chemistry and Physics* **13**, 12389-12404 (2013).

84. S. K. Schum, L. E. Brown, L. R. Mazzoleni, MFAssignR: Molecular formula assignment software for ultrahigh resolution mass spectrometry analysis of environmental complex mixtures. *Environmental Research* **191**, 110114 (2020).

85. G. W. Vandergrift, W. Kew, J. K. Lukowski, A. Bhattacharjee, A. V. Liyu, E. A. Shank, L. Paša-Tolić, V. Prabhakaran, C. R. Anderton, Imaging and direct sampling capabilities of nanospray desorption electrospray ionization with absorption-mode 21 Tesla Fourier transform ion cyclotron resonance mass spectrometry. *Analytical Chemistry* **94**, 3629-3636 (2022).

86. G. W. Vandergrift, A. S. M. Shawon, D. N. Dexheimer, M. A. Zawadowicz, F. Mei, S. China, Molecular Characterization of Organosulfate-Dominated Aerosols over Agricultural Fields from the Southern Great Plains by High-Resolution Mass Spectrometry. *ACS Earth and Space Chemistry* **6**, 1733-1741 (2022).

87. R. T. Kelly, J. S. Page, Q. Luo, R. J. Moore, D. J. Orton, K. Tang, R. D. Smith, Chemically etched open tubular and monolithic emitters for nanoelectrospray ionization mass spectrometry. *Analytical chemistry* **78**, 7796-7801 (2006).

88. N. M. Donahue, A. Robinson, C. Stanier, S. Pandis, Coupled partitioning, dilution, and chemical aging of semivolatile organics. *Environmental science & technology* **40**, 2635-2643 (2006).

89. Y. Li, U. Pöschl, M. Shiraiwa, Molecular corridors and parameterizations of volatility in the chemical evolution of organic aerosols. *Atmospheric Chemistry and Physics* **16**, 3327-3344 (2016).

90. S. A. Epstein, I. Riipinen, N. M. Donahue, A semiempirical correlation between enthalpy of vaporization and saturation concentration for organic aerosol. *Environmental science & technology* **44**, 743-748 (2010).

91. A. C. Doner, J. Zádor, B. Rotavera, Unimolecular Reactions of 2,4-Dimethyloxetanyl Radicals. *The Journal of Physical Chemistry A* **127**, 2591-2600 (2023).

92. N. S. Dewey, B. Rotavera, Chemical Kinetics Analysis of Cyclic Ether Species Profiles. *Combustion and Flame* **252**, 112753 (2023).

93. H. J. Curran, P. Gaffuri, W. J. Pitz, C. K. Westbrook, A comprehensive modeling study of n-heptane oxidation. *Combustion and flame* **114**, 149-177 (1998).

Author contributions:
Conceptualization: R.S., B.R., O.E.H., M.M.D., G.S.J.
Methodology: R.S., B.R., O.E.H, M.M.D., G.S.J, S.C., G.W.V.
Investigation: O.E.H., C.K.G., A.A., S.W.H., A.R.W., N.S.D., A.C.D., G.W.V., Z.C., M.M.D., G.S.J., Y.P.
Visualization: R.S., B.R., O.E.H., S.W.H.
Funding acquisition: R.S., B.R.
Writing – original draft: O.E.H., R.S., B.R., S.W.H.
Writing – review & editing: O.E.H., R.S., B.R., S.W.H., G.W.V., Z.C., S.C., M.M.D., G.S.J., Y.P.

Competing interests: Authors declare that they have no competing interests.

Data and materials availability: All data are available in the main text or the supplementary materials.